White Rose Research Online

eprints@whiterose.ac.uk
https://eprints.whiterose.ac.uk
Universities of Leeds, Sheffield and York

Deposited via The University of Sheffield.

White Rose Research Online URL for this paper:
https://eprints.whiterose.ac.uk/id/eprint/204629/

Version: Accepted Version

Article:
Verma, A.K., Ahmed, H., Burgos-Mellado, C. et al. (2023) Enhanced two consecutive samples based de-modulation technique for atomic force microscopy application. Measurement, 223. 113731. ISSN: 0263-2241

https://doi.org/10.1016/j.measurement.2023.113731

© 2023 The Authors. Except as otherwise noted, this author-accepted version of a journal article published in Measurement is made available via the University of Sheffield Research Publications and Copyright Policy under the terms of the Creative Commons Attribution 4.0 International License (CC-BY 4.0), which permits unrestricted use, distribution and reproduction in any medium, provided the original work is properly cited. To view a copy of this licence, visit http://creativecommons.org/licenses/by/4.0/

Reuse
This article is distributed under the terms of the Creative Commons Attribution (CC BY) licence. This licence allows you to distribute, remix, tweak, and build upon the work, even commercially, as long as you credit the authors for the original work. More information and the full terms of the licence here: https://creativecommons.org/licenses/

Takedown
If you consider content in White Rose Research Online to be in breach of UK law, please notify us by emailing eprints@whiterose.ac.uk including the URL of the record and the reason for the withdrawal request.

UNIVERSITY OF LEEDS
University of Sheffield
UNIVERSITY of York

Enhanced Two Consecutive Samples based De-modulation Technique for Atomic Force Microscopy Application

ARTICLE INFO

Keywords:
Amplitude estimation, Atomic force Microscopy, Delayed signal cancellation operators, Lyapunov's de-modulator, moving average filter (MAF)

ABSTRACT

This article investigates robust amplitude detectors suitable for atomic force microscopy (AFM) while discussing better alternatives. An AFM instrument's measurement unit is responsible for providing the amplitude information obtained from the tip of a cantilever beam to identify the surface smoothness of a test material. Therefore, two efficient approaches are suggested to leverage Lyapunov's theory while adhering to better noise suppression and DC-offset rejection capabilities. Nevertheless, an enhanced two samples-based Lyapunov's demodulation approach is proposed to detect the amplitude information rapidly. Consequently, the modifications applied to the conventional method help reduce the tuning efforts and structural complications. The proposed solution remains structurally simpler and useful for high- and low-frequency probes. Furthermore, the extensive design guidelines for all techniques and the simulation results are presented. Different amplitude signals are synthetically generated from several rough pseudo-test surfaces for early verification and sent to a real-time digital controller to judge the proposal's efficacy.

1. Introduction

High-resolution nano-scale imaging is often essential to characterize materials or biological samples for various research and industrial applications. In these cases, nanometer or lower spatial resolution of the characterized sample surfaces can provide researchers significant insight into the properties of the material. In recent times, atomic force microscopy (AFM) became a strong contender for nano-scale material surface characterization applications. Compared to similar other microscopy methods, AFM can provide atomic scale characterization with low-cost and ease of operation [1, 2, 3].

In the early days of AFM development, AFM was used to work in static mode, i.e., the cantilever probe is always in contact with surface and characterization is done from the interaction force between the probe and the sample. However, later on, dynamic mode was developed. This mode is also known as amplitude modulated AFM (AM-AFM). In AM-AFM, the cantilever oscillates at high frequency over the sample being characterized. By processing the cantilever deflection signal, a feedback controller performs the scanning of the material surface. Since the probe is not always in direct contact, this mode is more suitable to scan delicate samples owing to the low interaction force between the probe and the sample. Control-oriented dynamic mode AFM operation is detailed in [4, Fig. 1]. Interested readers may consult this reference for further details.

Cantilever deflection signal plays a fundamental role in ensuring high quality scanning by the AFM system. By estimating the amplitude of the scanned surface from the cantilever deflection signal, AFM controller can make sure that raster scanning is performed. Moreover, this also contributes to determine the overall imaging bandwidth of the scanning system since the estimated amplitude is used as the feedback signal to the controller. This highlights the importance of estimating the amplitude of the scanned surface from the cantilever deflection signal. Fast, accurate, and low-complexity amplitude estimation method will not only contribute to better scan quality, but also increase the overall imaging bandwidth of the system.

A simple but effective amplitude estimation method is the RMS-to-DC circuit [5]. This circuit can be implemented either in analog or digital domain. It works by integrating over a large number of samples. As such, the estimation speed is relatively slow. Traditionally, hardware lock-in-amplifiers (LIAs) [6, 7, 8, 9, 10, 11] are often used for the amplitude estimation purpose from the cantilever deflection signal. LIA exploits orthogonality property of the sinusoidal cantilever deflection signal. By multiplying the sinusoidal deflection signal with known frequency sine and cosine signals, LIA can easily estimate the amplitude. However, traditional LIA has low-bandwidth as high cut-off frequency low-pass filters (LPFs) are needed. To overcome this issue, high-bandwidth LIA was proposed in [12]. This approach is analogous to the synchronous reference frame phase-locked loop (SRF-PLL) [13] technique widely used in the power system literature. In [12], first an orthogonal signal is generated from the deflection signal. Then, the classical Park transformation [13] is applied. Thanks to the orthogonal signal and Park transformation, LIA in [12] require low cut-off frequency LPFs as opposed high cut-off frequency LPF in conventional LIAs. However, this approach is not suitable if the deflection signal has a DC component. In this case, additional filtering is required. Following similar line of investigation, discrete Fourier transform (DFT)-based LIA was proposed in [14]. Although this method has good performance, it requires real-time DFT implementation which can be computationally expensive. Similarly, the method in [15] enhanced the imaging bandwidth of LIA by employing four points-based estimation. This approach is often suitable for single-frequency sinusoidal signal. Extension to multi-frequency signal can be complicated. In addition to the electronic and/or software LIA, mechatronic LIA [16] is also proposed in the literature.

ORCID(s):

In recent times, two advanced amplitude estimation techniques are proposed in the AFM literature. They are Kalman filter [17, 18, 19, 20] and gradient a.k.a. Lyapunov estimator [21, 22, 23, 24]. By exploiting the noise properties of the signal, the Kalman filter can provide robust estimation of the amplitude. However, it is computationally expensive due to the presence of online matrix inversion. As such, the effective imaging bandwidth can be limited in practice. Gradient estimator is simple to implement and can extend the imaging bandwidth. However, in the presence of DC offset, the transient response can be sluggish. This motivated us to further improve the Lyapunov's estimator for AFM application.

As discussed, a conventional Lyapunov's demodulator (CLD) is a popularly accepted approach but require additional DC-offset feedback loop [21], which affects the amplitude tracking and noise elimination abilities. To overcome this drawback, the current proposal plays a better role in rapidly rejecting the DC-offset while having good noise suppression abilities confirming no significant modifications applied to the CLD approach. For this purpose, at first the possibilities to improve the CLD structure without using additional DC-offset feedback loop is explored. Accordingly, the need of employing additional noise filters is studied for further enhancing the noise suppression abilities, if required as per the AFM application environment. Unlike, the four samples [15] approach the proposed enhanced Lypunov's demodulator (ELD) relies on storing two samples which further enables to reduce additional memory requirements while enjoying it's usefulness for both the low and high frequency probe applications without applying significant tuning efforts.

2. Error Signal Demodulation Approaches

In this study, several improved estimators are presented for rapid detection of the amplitude information from a test surface, which are principally based on non-linear Lyapunov's estimation theory [21]–[23]. Note that high precision and reduced computational complexity are often needed for the sophisticated measuring instruments such as the AFM. There are several modes of operation suitable for an AFM instrument among which amplitude modulation mode emphasizes on accurate and fast detection of amplitude signal. In general, the signal obtained from a test surface under inspection is time varying and its envelop provides the amplitude information of a test surface. Consequently, the amplitude signal is itself a time varying variable in nature. The conventional amplitude detectors are capable to detect the amplitude signal but one has to compromise with the time response. For instance, let us consider a test signal along with DC-offset signal, as follows:

$$S(t) = A(t)\ \sin(\theta_o) + A_o \tag{1}$$

where $\theta_o = \int \omega_o\, dt = \omega_o t + \Phi$ is the known reference phase angle information based on the reference angular frequency adjusted prior to the measurement, i.e., ω_o, and Φ is the initial phase angle. The expansion of (1) upon applying the trigonometric identity, i.e. $\sin(A + B) = \sin(A)\cos(B) + \sin(B)\cos(A)$, is as follows:

$$S(t) = A(t)\cos(\Phi)\sin(\theta_o) + A(t)\sin(\Phi)\cos(\theta_o) + A_o \tag{2}$$

Equation (2) consist of two important components which we assume to be slowly time-varying and given by:

$$x_1 = A(t)\ \cos(\Phi) \tag{3}$$

$$x_2 = A(t)\ \sin(\Phi) \tag{4}$$

The accurate estimation of these components helps to estimate the amplitude information obtained from a test surface. Therefore, the estimated test signal can be re-written as follows:

$$\hat{S}(t) = \hat{x}_1\ \sin(\theta_o) + \hat{x}_2\ \cos(\theta_o) + \hat{A}_o \tag{5}$$

It is evident from the literature that the Laypunov demodulation (LD) [25] approach is the most attractive technique to estimate the signals, i.e. $\hat{x}_1$, $\hat{x}_2$ and $\hat{A}_o$ by simply applying the Laypunov's estimation law as given below:

$$\dot{\hat{x}}_1(t) = \sigma\ \sin(\omega_o t)\,(S(t) - \hat{S}(t)) = \sigma\ \sin(\omega_o t)\,\hat{e}_o \tag{6}$$

$$\dot{\hat{x}}_2(t) = \sigma\ \cos(\omega_o t)\,(S(t) - \hat{S}(t)) = \sigma\ \cos(\omega_o t)\,\hat{e}_o \tag{7}$$

$$\dot{\hat{A}}_o = \sigma_1\,(S(t) - \hat{S}(t)) = \sigma_1\,\hat{e}_o \tag{8}$$

where the positive tuning gains σ and σ_1 can be chosen as $\sigma = 8\,\omega_o/2\pi$ and $\sigma_1 = \omega_o/2\pi = \sigma/8$ according to [21]–[23]. The conventional Lyapunov's de-modulator (CLD) obtained from Equations (6)–(8) is depicted in Fig 1.

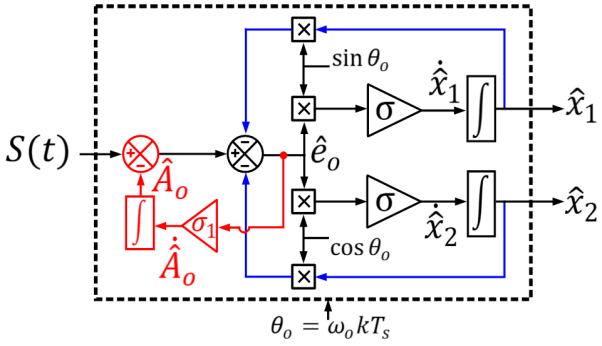


Figure 1: Generic Lyapunov's demodulator with DC-offset rejection loop.

The state-space model for the CLD can be expressed as:

$$\begin{bmatrix} \dot{\hat{x}}_1 \\ \dot{\hat{x}}_2 \\ \dot{\hat{A}}_o \end{bmatrix} = \underbrace{\begin{bmatrix} \sin(\omega_o t) & \cos(\omega_o t) & 1 \end{bmatrix}^T}_{\mathbf{H}} \cdot \begin{bmatrix} 1 \\ 1 \\ 1/8 \end{bmatrix} \sigma\, \hat{e}_o \tag{9}$$

$$\hat{S} = \mathbf{H}^T \begin{bmatrix} \hat{x}_1 & \hat{x}_2 & \hat{A}_o \end{bmatrix}^T \tag{10}$$

It requires attention that the signal vector $\mathbf{H}$ follows persistent excitation (PE) property and the strictly positive

real Lyapunov design approach along with the Kalman-Yakubovich-Popov and Meyer-Kalman-Yakubovich Lemmas in order to ensure the stability of Lyapunov's estimation law. Besides this fact, the errors in the estimation are presented to determine the boundedness of the estimated states as follows:

$$\begin{aligned}\tilde{x}_1 &= x_1 - \hat{x}_1\\ \tilde{x}_2 &= x_2 - \hat{x}_2\\ \tilde{A}_o &= A_o - \hat{A}_o\end{aligned} \tag{11}$$

Using (11), the term $\hat{e}_o$ can be expressed as:

$$\hat{e}_o = \tilde{x}_1 \ \sin(\omega_o t) + \tilde{x}_2 \ \cos(\omega_o t) + \tilde{A}_o \tag{12}$$

As per the previously mentioned lemmas, a Lyapunov-like function can be chosen as follows:

$$X_{LP}(t) = \frac{\tilde{x}_1^2(t) + \tilde{x}_2^2(t) + 8\tilde{A}_o^2}{2} \tag{13}$$

The time derivative of (13) is:

$$\dot{X}_{LP}(t) = \tilde{x}_1\dot{\tilde{x}}_1 + \tilde{x}_2\dot{\tilde{x}}_2 + 8\tilde{A}_o\dot{\tilde{A}}_o \tag{14}$$

where $\dot{\tilde{x}}_1$=$-\dot{\hat{x}}_1$, $\dot{\tilde{x}}_2$=$-\dot{\hat{x}}_2$ and $\dot{\tilde{A}}_o$=$-\dot{\hat{A}}_o$. Similarly, the time derivatives are further expressed as follows:

$$\begin{aligned}\dot{\hat{x}}_1 &= -\sigma \sin(\omega_o t)\hat{e}_o\\ \dot{\hat{x}}_2 &= -\sigma \cos(\omega_o t)\hat{e}_o\\ \dot{\hat{A}}_o &= -\sigma/8\hat{e}_o\end{aligned} \tag{15}$$

A non-positive $\dot{X}_{LP}(t)$ is confirmed as follows:

$$\dot{V}_{LP}(t) = -\sigma\left(\tilde{x}_1 \ \sin(\omega_o t) + \tilde{x}_2 \ \cos(\omega_o t) + \tilde{A}_o\right)\hat{e}_o = -\sigma\,\hat{e}_o^2 \tag{16}$$

For $\sigma > 0$ along with the PE property [21],[26], $\dot{V}_{LP}(t) \leq 0$, helps in confirming that the estimated state variables are settled to the actual values as follows:

$$\begin{aligned}\lim_{t\to\infty} &= \hat{x}_1 = x_1\\ \lim_{t\to\infty} &= \hat{x}_2 = x_2\\ \lim_{t\to\infty} &= \hat{A}_o = A_o\end{aligned} \tag{17}$$

A guaranteed boundedness can be ensured without any steady-state error. To effectively estimate $\hat{A}_o$, the tuning gain parameter (σ_1) must be lower than the actual value of σ [25]. Since the DC-offset is a low-frequency component whose elimination requires a narrow bandwidth loop resulting in a slower dynamic response.

2.1. Small-Signal Model Development for the CLD Method

The Lyapunov function-based stability analysis approach presented above is very suitable to assess stability. However, the gain tuning and/or frequency-domain analysis is more complex to obtain, which is very useful for practical implementation and analyzing the frequency-domain stability of the CLD method. This void is addressed here through small-signal model development. For further progression in this section, we will extensively use the small-angle approximation approach, i.e., $\sin(\theta) \approx \theta$ and $\cos(\theta) \approx 1$. Moreover, we assume quasi-locked condition, i.e., $A \approx \hat{A}$, $A_0 \approx \hat{A}_0$, and $\Phi \approx \hat{\Phi}_0$ [27]. These assumptions imply that we are working close to the zero estimation error vicinity, i.e., the equilibrium point in which the small-signal model is developed. This is essential to obtain a linear model for a nonlinear estimator given by eqs. (6)-(8). Using the estimated variables $\hat{x}_1$ and $\hat{x}_2$, the amplitude can be estimated as $\hat{A} = \sqrt{\hat{x}_1^2 + \hat{x}_2^2}$ and the dynamics are computed as:

$$\dot{\hat{A}} = \frac{\hat{x}_1\dot{\hat{x}}_1 + \hat{x}_2\dot{\hat{x}}_2}{\sqrt{\hat{x}_1^2 + \hat{x}_2^2}}. \tag{18}$$

By substituting eqs. (6) and (7) together with eqs. (1)-(5) in eq. (18), one can obtain that:

$$\begin{aligned}\dot{\hat{A}} &= \frac{\hat{x}_1\sigma\sin(\omega_o t)\left(S - \hat{S}\right) + \hat{x}_2\sigma\cos(\omega_o t)\left(S - \hat{S}\right)}{\sqrt{\left(\hat{A}\cos\left(\hat{\Phi}\right)\right)^2 + \left(\hat{A}\sin\left(\hat{\Phi}\right)\right)^2}},\\ &= \frac{\sigma\hat{A}\sin\left(\hat{\theta}_0\right)\left(S - \hat{S}\right)}{\hat{A}},\\ &= \sigma\sin\left(\hat{\theta}_0\right)\left(A_0 + A\sin\left(\theta_0\right) - \hat{A}_0 - \hat{A}\sin\left(\hat{\theta}_0\right)\right),\\ &= \frac{\sigma}{2}\left[A\cos\left(\theta_0 - \hat{\theta}_0\right) - A\cos\left(\theta + \hat{\theta}_0\right) + \right.\\ &\quad \left.\cos\left(2\hat{\theta}_0\right) - \hat{A}\right] + \sigma\left(A_0 - \hat{A}_0\right)\cos\left(\hat{\theta}_0\right).\end{aligned} \tag{19}$$

Applying the small-signal approximation to eq. (19), this equation can be simplified as:

$$\dot{\hat{A}} \approx \frac{\sigma}{2}\left(A - \hat{A}\right) + \sigma\left(A_0 - \hat{A}_0\right). \tag{20}$$

Similarly, the DC-offset estimation dynamics (eq. (8)) can be rewritten as:

$$\begin{aligned}\dot{\hat{A}}_0 &= \sigma_1\left(A_0 + A\sin\left(\theta_0\right) - \hat{A}_0 - \hat{A}\sin\left(\hat{\theta}_0\right)\right),\\ &= \sigma_1\left(A_0 - \hat{A}_0\right) +\\ &\quad \sigma_1\left(A\sin\left(\theta_0\right) - \hat{A}\sin\left(\hat{\theta}_0\right)\right).\end{aligned} \tag{21}$$

Applying small-signal approximation to eq. (21) and assuming $A \approx \hat{A} \approx 1$, the eq. (21) can be simplified as:

$$\dot{\hat{A}}_0 \approx \sigma_1\left(A_0 - \hat{A}_0\right) + \sigma_1\left(\Phi - \hat{\Phi}\right). \tag{22}$$

Initial phase angle can be estimated as $\hat{\Phi} = \arctan\left(\hat{x}_2/\hat{x}_1\right)$. Then, the dynamics can be obtained as:

$$\begin{aligned}\dot{\hat{\Phi}} &= \frac{\hat{x}_1\dot{\hat{x}}_2 - \hat{x}_2\dot{\hat{x}}_1,}{\hat{x}_1^2 + \hat{x}_2^2}\\ &= \frac{\hat{x}_1\sigma\cos(\omega_o t)\left(S - \hat{S}\right) - \hat{x}_2\sigma\sin(\omega_o t)\left(S - \hat{S}\right)}{\hat{A}^2},\\ &= \sigma\frac{\cos\left(\hat{\theta}_0\right)\left(A_0 + A\sin\left(\theta_0\right) - \hat{A}_0 - \hat{A}\sin\left(\hat{\theta}_0\right)\right)}{\hat{A}},\\ &= \sigma\frac{\cos\left(\hat{\theta}_0\right)\left(A\sin\left(\theta_0\right) - \hat{A}\sin\left(\hat{\theta}_0\right)\right)}{\hat{A}} +\end{aligned}$$

$$+\sigma\frac{\cos\left(\hat{\theta}_0\right)\left(A_0-\hat{A}_0\right)}{\hat{A}}. \tag{23}$$

The second term in eq. (23) can be simplified using small-angle approximation and assuming $\hat{A}\approx 1$ as $\sigma\left(A_0-\hat{A}_0\right)$. Moreover, the first-term in eq. (23) can also be approximated as:

$$\begin{aligned}&\sigma\frac{\cos\left(\hat{\theta}_0\right)\left(A\sin\left(\theta_0\right)-\hat{A}\sin\left(\hat{\theta}_0\right)\right)}{\hat{A}}\\&\approx\sigma\left(\theta_0-\hat{\theta}_0\right)\\&\approx\sigma\left(\Phi-\hat{\Phi}_0\right).\end{aligned} \tag{24}$$

As a result, eq. (24) can be approximated as:

$$\dot{\hat{\Phi}}\approx\sigma\left(\left(\Phi-\hat{\Phi}_0\right)+\left(A_0-\hat{A}_0\right)\right). \tag{25}$$

Equations (20), (22), and (25) represent the small-signal model of the CLD method. These equations show that the estimation dynamics of amplitude, DC-offset, and initial phase angle not only depend on these variables itself but also other variables. These cross-coupling effects make it difficult to obtain individual transfer functions that can be utilized for gain tuning and stability analysis. The main variable of interest in this work is the estimated amplitude, which is then used for characterizing the surface of the material sample.

Equation (20) show that the amplitude estimation dynamics depends also on the DC-offset estimation error. Typically, DC-offset's amplitude is significantly smaller than the signal amplitude. As such, the DC-offset estimation error, i.e., the second term in eq. (20) will be significantly smaller and can locally be ignored. Then, eq. (20) can be approximated as

$$\dot{\hat{A}}\approx\frac{\sigma}{2}\left(A-\hat{A}\right). \tag{26}$$

Applying Laplace transformation to eq. (26), the amplitude estimation dynamics transfer function can be obtained as:

$$\frac{\hat{A}}{A}(s)=\frac{\frac{\sigma}{2}}{s+\frac{\sigma}{2}}. \tag{27}$$

Transfer function (27) shows that the amplitude estimation dynamics works as a low-pass filter and the cut-off frequency is selected by the tuning gain σ. Transfer function (27) is obtained by ignoring the DC-offset estimation dynamics, and consequently the DC-offset estimation dynamics gain σ_1. As such, validity of this transfer function depends on small-amplitude DC-offset only. If the DC-offset amplitude is sufficiently high, this will invalidate the transfer function. Moreover, transfer function (27) can be used for tuning the gain σ not the DC-offset estimation gain σ_1.

According to Fig. 1, the DC-offset estimation loops acts as an outer-loop, whereas the amplitude estimation loop is the inner-loop. To ensure the system stability, the outer-loop has to be slower than the inner-loop, which is evidenced by the significantly smaller value selection for σ_1 compared to σ. As such, there is a trade-off in selecting the gains for the conventional Lyapunov demodulator.

To mitigate the effect of cross-coupling terms in the amplitude dynamics and consequently the stability of conventional Lyapunov demodulator, two improved demodulators are proposed in this work. In the first approach, DC-offset-induced estimation error is mitigated through in-loop filtering. In the second approach, the DC-offset is rejected outside the amplitude estimation loop, i.e., through a pre-loop filter. Both approaches overcome the effect of cross-coupling terms in the amplitude estimation dynamics, which results in improving the stability of the CLD.

2.2. Improved CLD approach

For the previously mentioned reason, possible improved approaches may require attention for dynamic performance improvement of an AFM instrument. It is advantageous and important to have the rejection of both the DC-offset and the noisy components simultaneously from an amplitude signal. In order to achieve this goal, good efforts are required to get rid of the sluggish DC-offset rejection loop from the structure of CLD. In Fig. 2, an improved proposal is reported in [28] for power system applications consisting of either moving average filters (MAF) or delayed signal cancellation (DSC) operators, denoted by $G(s)$ may be employed. Herein,

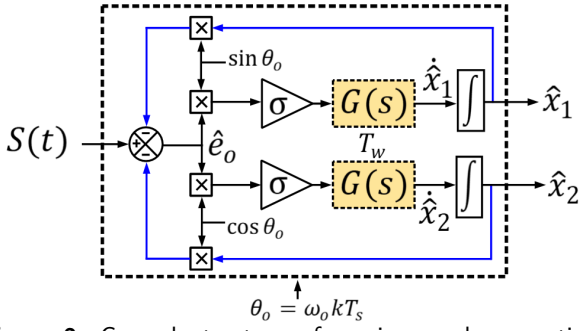


Figure 2: General structure of an improved conventional Lyapunov's de-modulator based amplitude detector.

the choice of the aforementioned filters can affect the following: structural complexity, dynamic response time and the noise suppression abilities. Hence, the objective of this work is to obtain efficient CLD architectures while highlighting the pros and cons for AFM application. Thus, the issues are sub-divided and investigated accordingly in the ensuing subsections.

2.3. Elimination of DC-Offset rejection loop

In this section, the removal of DC-offset rejection loop is emphasized. From the improved conventional LD (ICLD) (see Fig. 2), assuming $G(s)=1$, leads to a CLD without a DC-offset rejection loop. Therefore, CLD will become sensitive to DC-offset component present in the amplitude signal obtained from a cantilever beam. Let us now consider the Equations (1) and (5), then the error signal is,

$$\hat{e}_D=\hat{e}_o+A_o \tag{28}$$

Note that, mathematically the term $\hat{A}_o$ will be absent in Equation (5). After applying demodulation, the state variables $\dot{\hat{x}}_1$ and $\dot{\hat{x}}_2$ are obtained as:

$$\dot{\hat{x}}_1=\sigma\sin(\omega_o t)\hat{e}_D=\sigma\ \sin(\omega_o t)\ \hat{e}_o+\sigma\ A_o\ \sin(\omega_o t)$$

$$\dot{\hat{x}}_2 = \sigma \cos(\omega_o t)\hat{e}_D = \sigma\ \cos(\omega_o t)\,\hat{e} + \sigma\ A_o\ \cos(\omega_o t) \tag{29}$$

The component A_o will induce full-cycle oscillations in $\hat{x}_1$ and $\hat{x}_2$ components with the choice of reference frequency f_o. Therefore, the low-pass filters, i.e. MAF and DSC operators are beneficial over a sluggish DC-offset rejection loop. The continuous-time transfer functions for MAFs and DSC operators which may be plugged into $G(s)$, are as follows:

$$G(s) = G_{MAF}(s) = \frac{1 - e^{-T_w s}}{T_w s} \tag{30}$$

$$G(s) = G_{DSC}(s) = \frac{1 + e^{-T_w s/2}}{2} \tag{31}$$

Note that the window length (T_w) is T_w=T_o, where $T_o = 1/f_o$. In view of the digital implementation of the amplitude detectors, using bi-linear transformation [29], the discrete time realization of the filters is as follows:

$$G_{MAF}(z) = \frac{1}{N}\frac{1 - z^{-N}}{1 - z^{-1}} \tag{32}$$

$$G_{DSC}(z) = \frac{1 + z^{-N/2}}{2} \tag{33}$$

where, $N = T_w/T_s$ and T_s are the number of samples and the sampling time period, respectively. Assuming a sampling frequency (f_s) of interest is 200 kHz and reference frequency (f_o) of 20 kHz [21], a bode response plot is depicted in Fig. 3 to demonstrate the usefulness of the proposed filters in ICLD structure for elimination of DC-offset component. The structure involving MAF is identified as ICLD-M and

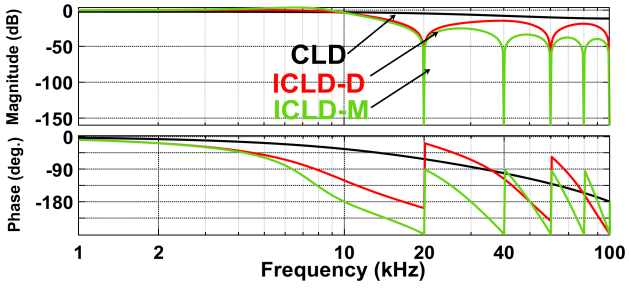


Figure 3: Bode response plots of CLD, ICLD-M and ICLD-D.

the structure with DSC operator is identified as ICLD-D. Note that both the structures behave as a comb filter like structure. This ensures that the designer can tweak the filter properties and can avoid the sluggish DC-offset rejection loop. Furthermore, the estimation of amplitude signal can be carried out using $\hat{A}_1 = \sqrt{\hat{x}_1^2 + \hat{x}_2^2}$. Therefore, in a simulation environment (see Fig. 4), the signal $S(t)$ contaminated with 40% of DC-offset along with a 50% step change in amplitude is applied to all the amplitude detectors discussed so far. It can be seen that all the amplitude detectors are able to track the amplitude signal. However, the CLD shows an oscillatory behavior and takes longer time to settle when compared to ICLD-M/D structures.

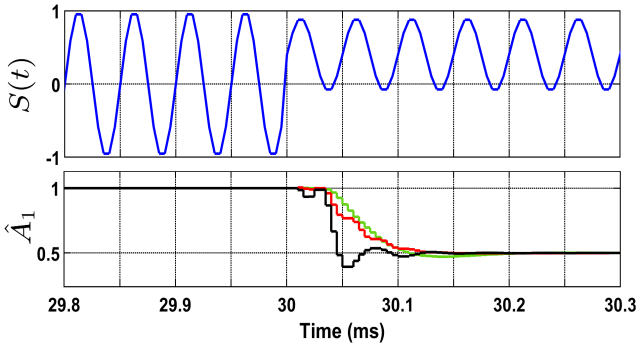


Figure 4: Amplitude tracking performance of CLD, ICLD-M and ICLD-D.

2.4. Noise elimination and reduction in structural complexities

A noise signal when coupled with the amplitude signal might affect the accuracy of AFM instrument while conducting an experiment on a test surface in noisy conditions. Therefore, the measurements obtained from an AFM instrument will always lie in a region of certain approximation. To explore the aforesaid concern, let us consider a third harmonic component as a noisy component which is coupled with the eq. (1). For the sake of simplicity A_o is considered absent in eq. (1). Thus, the noise affected test signal is,

$$\begin{aligned} S_n(t) &= S(t) + S_3(t) \\ &= A(t)\sin(\omega_o t + \Phi) + A_3(t)\sin(3\omega_o t + \Phi_3) \end{aligned} \tag{34}$$

where, $A_3(t)$ is the amplitude and Φ_3 is the initial phase of the third harmonic component. The error signal generated in this case is as follows:

$$\hat{e}_n = \hat{e}_o + S_3(t) \tag{35}$$

Using Lyapunov's estimation law, the state variables, i.e. $\dot{\hat{x}}_1$ and $\dot{\hat{x}}_2$ are contaminated with unwanted even harmonic components and are re-written as follows:

$$\begin{aligned} \dot{\hat{x}}_1 &= \sigma\ \sin(\omega_o t)\,\hat{e}_o + \sigma \overbrace{S_3(t)\ \sin(\omega_o t)}^{X} \\ \dot{\hat{x}}_2 &= \sigma\ \cos(\omega_o t)\,\hat{e}_o + \sigma \underbrace{S_3(t)\ \cos(\omega_o t)}_{Y} \end{aligned} \tag{36}$$

The evaluation of the terms 'X' and 'Y' yields:

$$\begin{aligned} S_3(t)\ \sin(\omega_o t) &= \frac{A_3}{2}[\cos(2\,\omega_o\,t) - \cos(4\,\omega_o\,t)] \\ S_3(t)\ \cos(\omega_o t) &= \frac{A_3}{2}[\sin(2\,\omega_o\,t) + \sin(4\,\omega_o\,t)] \end{aligned} \tag{37}$$

The coupling of even-harmonic terms with the $\hat{x}_1$ and $\hat{x}_2$ leads to an inaccurate estimate of amplitude. Hence, the inclusion of low-pass filter such as MAFs and DSC operators can be an effective choice in simultaneous rejection of noise and DC-offset components.

2.5. Small-Signal Modeling of the ICLD Method

The error demodulation approach is simply an equivalence to Park's transformation [28] employed for phase-locked loops algorithms wherein stationary reference ($\alpha\beta$)

frame components are transformed into rotating reference (dq) frame components. The estimated states variables ($\hat{x}_1$ and $\hat{x}_2$) are treated as DC-variables in $dq-$frame. Using small angle approximation, if $\Phi \rightarrow 0$ then $\sin(\Phi) \approx 0$ and $\cos(\Phi) \approx 1$, therefore, the state variables are expressed as follows:

$$\hat{x}_1 \approx A(t) \tag{38}$$

$$\hat{x}_2 \approx 0 \tag{39}$$

This simply states that the designer might not have to deal with both the components and/or the mathematical square root operation. Since only $\hat{x}_1$ state is enough to estimate the amplitude signal. The small signal model for the ICLD structure is shown in Fig. 5. Note that the factor of '1/2' is

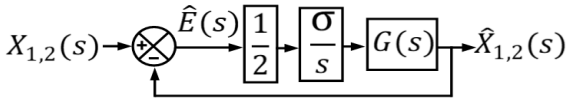


Figure 5: Small signal model of ICD

included in the models, as the error signal is equally divided into two parts. The transfer function relationship for ICLD structure is obtained as follows:

$$\frac{\hat{X}_{1,2}(s)}{X_{1,2}(s)} = \frac{\hat{X}_1(s)}{X_1(s)} = \frac{\hat{X}_2(s)}{X_2(s)} = \frac{G(s)}{\left(\frac{s}{\omega_p}\right) + G(s)} \tag{40}$$

where $\omega_p = \sigma/2$ is the cut-off frequency. Note that the transfer function of the improved conventional Lyapunov demodulator given by eq. (40) is the same as the conventional Lyapunov demodulator transfer function given by eq. (27) when $G(s) = 1$. However, unlike the conventional method, the improved one did not exclude the DC-offset estimation dynamics as the DC-offset induced estimation error is mitigated by the transfer function $G(s)$. As such, stability analysis and tuning of the improved Lyapunov demodulator can be easily done using well-known methods from the linear system theory. Moreover, by making an appropriate choice of the transfer function $G(s)$, it is possible to enhance the stability, unlike the conventional counterpart. In addition, the gain σ and the transfer function $G(s)$ can be independently tuned without compromising the stability, unlike the conventional Lyapunov demodulator. In order to design σ, consider $G(s) = 1$ in (40) and obtain the CLD structure, with an appropriate choice of σ, the bandwidth of the CLD structure can be varied till a satisfactory trade-off in dynamic response time and noise attention abilities is obtained [25].

3. Proposed Two Consecutive Samples Based Amplitude Estimation

The knowledge gained from the filter properties of the ICLD structure, it is to be recalled that the estimation of $\hat{x}_1$ and $\hat{x}_2$ states is still slower in response. Therefore, a two consecutive samples based amplitude detector is proposed. Using only two consecutive samples of the amplitude signal, an error signal can be generated while rapid rejection of the DC-offset component can be ensured. Let us try to obtain the error signal from an amplitude signal given below:

$$S(t) = A(t)\ \sin(\omega_o t + \Phi) + A_o \tag{41}$$

The delayed version of $S(t)$ is obtained as:

$$S(t-\tau) = A(t-\tau)\ \sin(\omega_o t + \Phi - \tau\omega_o) + A_o \tag{42}$$

The error signal is obtained as follows:

$$\hat{e}_o = \frac{S(t) - S(t-\tau)}{2\Delta t} \tag{43}$$

where, τ and Δt are equivalent to T_o and T_s, respectively. The estimated amplitude can be obtained as follows:

$$\dot{\hat{x}}_1 = f_o\ \sin(\omega_o t)\ \hat{e}_o \tag{44}$$

The block diagram of the current proposal is shown in Fig. 6. The proposed amplitude estimator can be employed

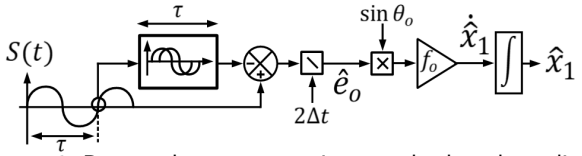


Figure 6: Proposed two consecutive samples based amplitude detector

for both low and high-frequency probes. In a simulation environment, four consecutive samples (FCS) [15] and the proposed two consecutive samples (2CS) based amplitude estimators are compared at both low and high frequencies. In Fig 7, a 20 kHz input signal "$S(t)$" along with a square amplitude modulation of 1 kHz is applied to both the amplitude estimators. It can be observed that the FCS is not a feasible

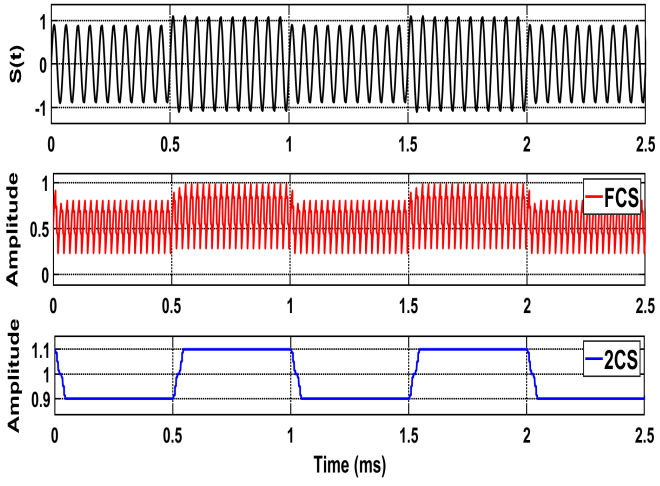


Figure 7: Amplitdue tracking performance for low frequency probes.

solution for low frequency probes. On the other hand, when a 10 MHz input signal "$S(t)$" along with a square amplitude

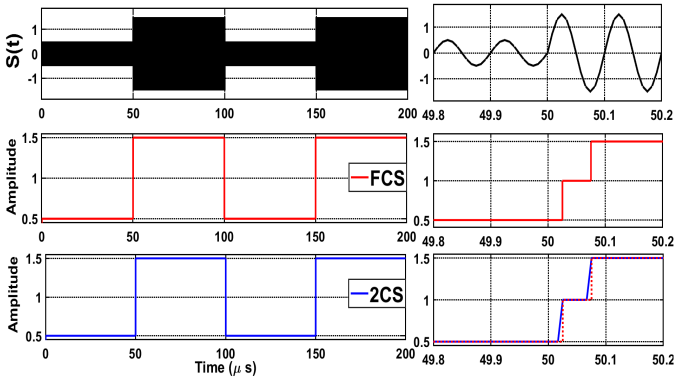


Figure 8: Amplitdue tracking performance for high frequency probes with close-up view on right-hand side.

modulation of 10 kHz is applied to both the amplitude estimators, as shown in Fig. 8. It is clearly visible from zoom view (see Fig. 8) that both the amplitude estimators take equal amount of settling time i.e. one fundamental cycle with a similar kind of dynamic response behavior. From the bode plot (see Fig. 9), note that the proposed

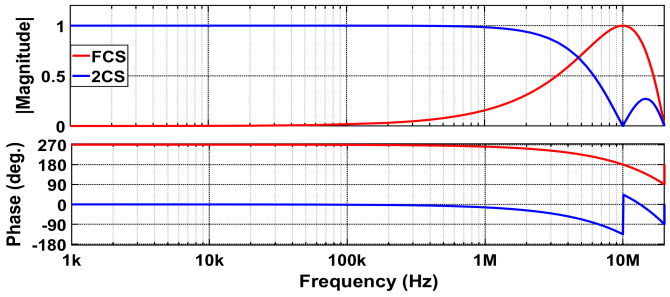


Figure 9: Bode reponse plots of FCS and 2CS amplitude estimators.

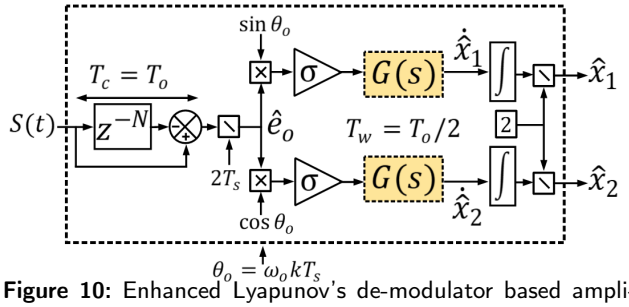


Figure 10: Enhanced Lyapunov's de-modulator based amplitude detector.

2CS offers unity gain in low-frequency region whereas FCS offers zero gain, illustrating the fact that the FCS technique is unsuitable for low frequency operation. Nevertheless, some of the architectural properties of the proposed 2CS approach are identical to the ICLD. Thus, an enhanced Lyapunov demodulator (ELD) structure can be derived which make use of a transport delay block to avoid the state feedback approach for error signal generation similar to the case of ICLD and CLD structures (see Fig. 10). If required, low-pass filters ($G(s)$) such as MAFs and DSCs operators can be employed to further improve the noise immunity in case of the ELD. The discrete time transfer function of the transport delay block can be realized as follows:

$$T(z) = \frac{\hat{E}(s)}{S(s)} = \frac{1 - z^{-N}}{2T_s} \tag{45}$$

where, $N = \tau/\Delta t$. This ensures that the window length (T_c) is equivalent to N samples required to enforce the $\hat{e}_o$ toward zero as well as rejection of DC-offset component. In Fig. 11, a bode plot is exemplified to confirm the DC-offset rejection ability of the ELD structure. Further, the demodulation of

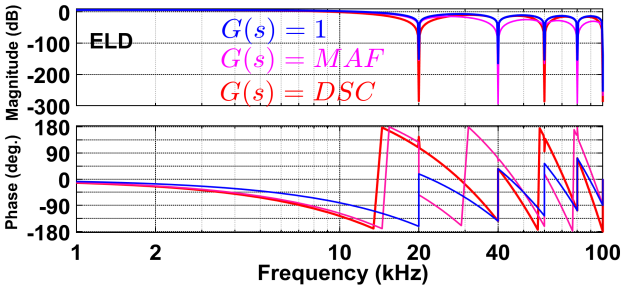


Figure 11: Bode response plots for ELD structures.

error signal will become simpler to implement and the state variables, i.e. $\dot{\hat{x}}_1$ and $\dot{\hat{x}}_2$ converge to $\hat{x}_1$ and $\hat{x}_2$ rapidly after N samples of delay without employing a state-feedback approach. Furthermore, an adequate amount of filtering is also offered by transport delay block alone considering $G(s)$=1. In order to provide better immunity against noise, $G(s)$ in ELD structure may be replaced with the MAFs and/or DSC operators as:

$$G_{MAF}(z) = \frac{2}{N}\frac{1 - z^{-N/2}}{1 - z^{-1}} \tag{46}$$

$$G_{DSC}(z) = \frac{1 + z^{-N/2}}{2} \tag{47}$$

A minor difference between ELD-M structure and ICLD-M structure is, N samples are required by the MAFs in ICLD-M structure and $N/2$ samples are required by the MAFs in ELD-M structure. Also, with regard to the DSC operators, both the ELD-D and ICLD-D needs $N/2$ samples. For high-

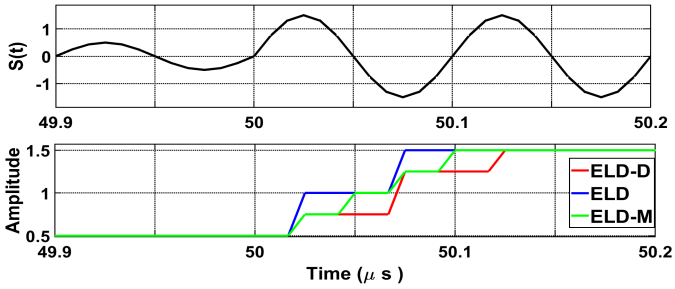


Figure 12: Dynamic behavior comparison of the ELD structures when $G(s) = 1$ is replaced by $G_{MAF}(s)$ and $G_{DSC}(s)$ filters.

frequency probes, the dynamic performance of the proposed ELD structures is compared in Fig. 12. It can be inferred that all the estimators possess good steady-state accuracy with slight differences in settling time abilities. Furthermore, the

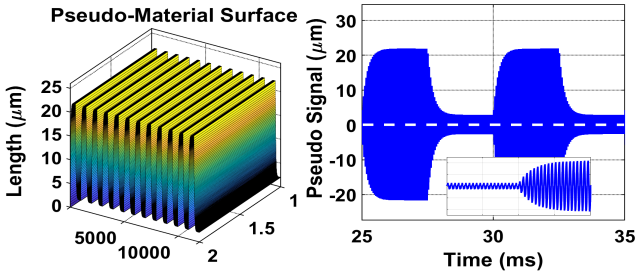
overall transfer function relationship for an ELD structure is straightforward to deduce using the small-signal modeling approach applied to ICLD structure, as follows:

$$\frac{\hat{X}_{1,2}(s)}{X_{1,2}(s)} = \frac{T(s)\,G(s)}{\left(\frac{s}{\omega_p}\right)} \tag{48}$$

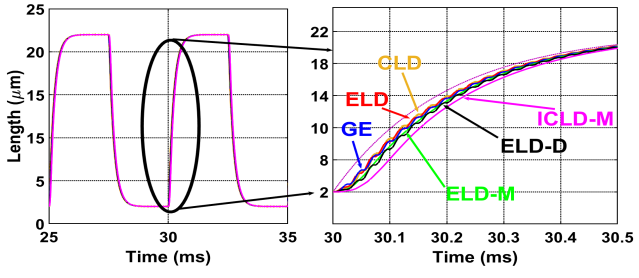
where, $T(s)$ and $G(s)$ are s-domain transfer functions of the transfer delay block and the MAF/DSC filters, respectively.

4. Simulation Results For Pesudo-Test Surfaces

In Matlab/Simulink environment, four pseudo-test surfaces are generated which are in near proximity to the actual test surfaces. The generated test signal is then provided to six potential amplitude detectors, i.e. the conventional Lyapunov's demodulator (CLD) [21], the gradient descent estimator (GE) [23], the improved CLD with $G_{MAF}(s)$ is denoted as ICLD-M [28] which are compared with the proposed approach. The different variants of the proposed ELD structures are as follows: the first variant without filter ($G(s) = 1$) is denoted as ELD, the second variant with a moving average filter ($G_{MAF}(s)$) is denoted as ELD-M and the third variant with a delayed signal cancellation operator ($G_{DSC}(s)$) is denoted by ELD-D. The test input signal frequency is considered 20 kHz, and the sampling frequency is 200 kHz. A pseudo-material surface having equal spaces with a height of 20 μm along with its equivalent amplitude signal is exemplified in Fig. 13(a). Moreover, the



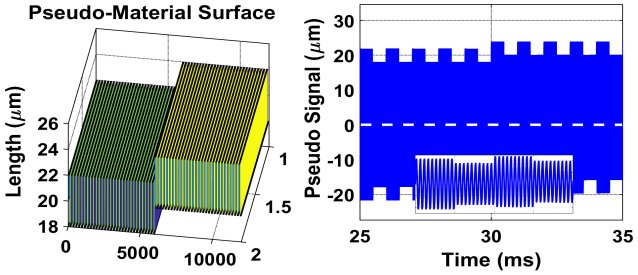
(a) Pseudo-equally spaced surface and it's equivalent input signal



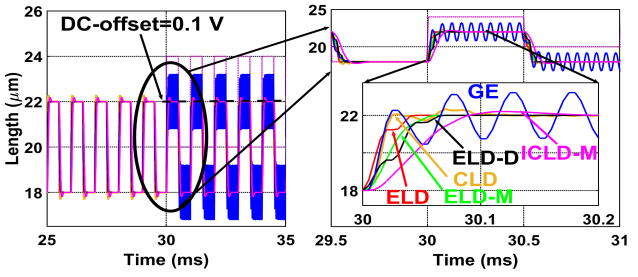
(b) Amplitude estimation

Figure 13: Amplitude estimation for an equally spaced pseudo-surface

input signal has a slower rise time and fall time whose impact on amplitude tracking abilities of different estimators is shown in Fig. 13(b). The structures such as ELD, CLD, GE, and ELD-M/D are closer to the reference amplitude signal when compared to ICLD-M. However, a smoother dynamic response is obtained with the ICLD-M amplitude detector when compared to all other estimators. Nevertheless, the



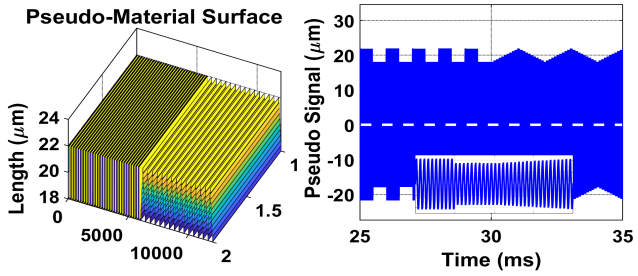
(a) Input signal with DC-offset



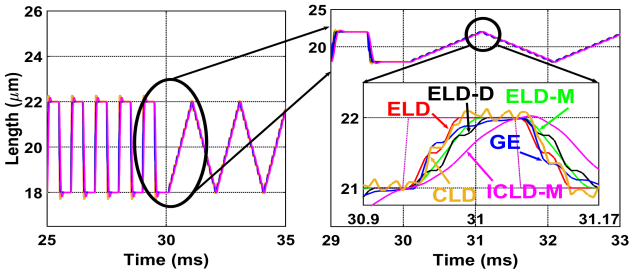
(b) Amplitude estimation in the presence of DC-offset

Figure 14: Dynamic amplitude tracking performance.

malfunctioning of the analogue-to-digital converter of an AFM instrument might lead to the existence of a DC-offset component in the measurement, as shown in Fig.14(a). It is observed in Fig. 14(b), that the GE is incapable of handling the DC-offset component present in the amplitude signal. Note that a fast dynamic response is obtained with the ELD and ELD-M/D structures without any error when compared to the CLD structure. On the other hand, a slower and smoother dynamic response is obtained with the ICLD-M structure owing to the existence of MAF filters. In practice,



(a) Input signal with triangular amplitude modulation



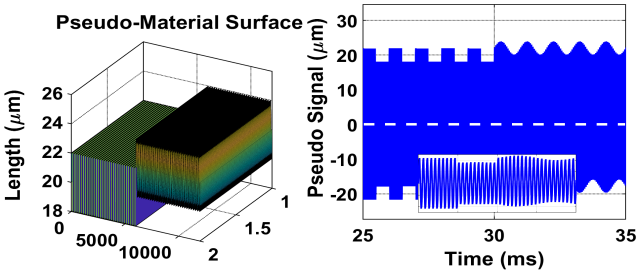
(b) Amplitude estimation of a triangular envelop

Figure 15: Amplitude tracking performance for a pseudo triangular surface

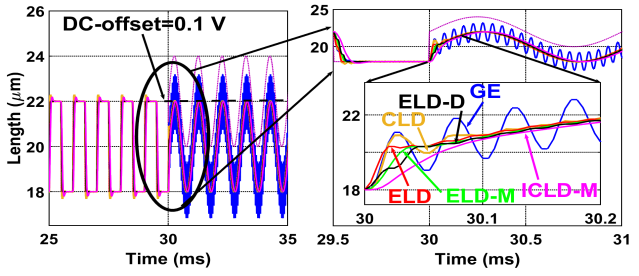
Table 1
Comparative analysis of key metrics for different amplitude estimators

Key parameters	Amplitude Estimators			
	CLD [25]	GE [23]	2CS [15]	ELD
DC-offset Elimination Ability	√	×	×	√
Noise Rejection ability	Good	Average	Poor	Better
High-Frequency Application	×	×	√	√
Low Frequency Application	√	√	×	√
Steady-state Accuracy	Good	Good	Better	Better
Control Complexity	Higher	Medium	Least	Medium

the test surfaces are not smooth in nature and possible slow variations may occur in the surface. For example, a triangular amplitude-modulated signal (see Fig. 15) and sinusoidal amplitude-modulated signal along with DC-offset (see Fig. 16) are considered to evaluate the robustness of the proposed amplitude detectors. The ELD estimator and



(a) Sinusoidal amplitude modulated input signal with DC-offset



(b) Rejection of DC-offset while estimating sinusoidal envelop

Figure 16: Sinusoidal amplitude tracking performance

its derivatives outperform in terms of following the mean value of the reference amplitude signal compared to other amplitude estimators without any steady-state errors. It is evident that all the estimators can effectively track the ramping and sinusoidal variations, among which ELD proves to be a dynamically faster and more accurate approach for AFM application.

5. Experimental Results

This section compares the proposed ELD estimator with conventional Lyapunov's demodulator [25] and gradient estimator [23] to assess the real-time applicability. For this purpose, the pseudo-surface signal is generated internally through the use of a digital-to-analogue converter (DAC)

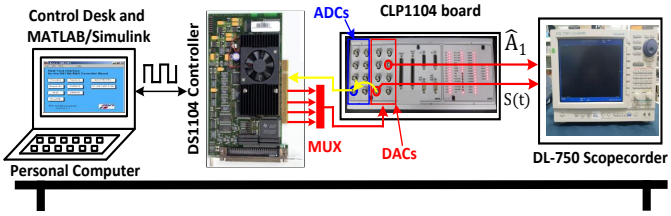
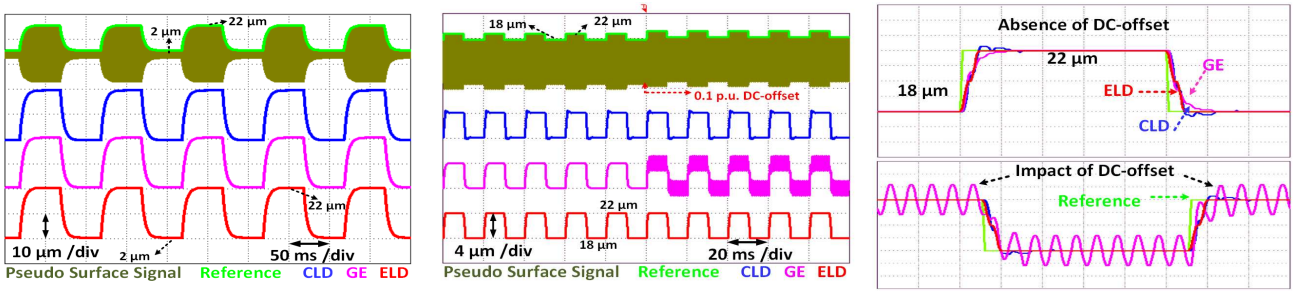


Figure 17: Experimental rig for early verification of amplitude estimators

port of a dSPACE (DS1104) controller card, which is sampled at 10 kHz as shown in Fig. 17. The amplitude estimators are implemented using a discrete-time solver in a MATLAB/Simulink environment. The control algorithms will receive pseudo-surface signals through an analogue-to-digital converter (ADC) port, and the estimated amplitude signals and pseudo-surface signals are captured on a DL-750 ScopeCorder. In Fig. 18 and Fig. 19, four test cases are presented, which are organized as follows:

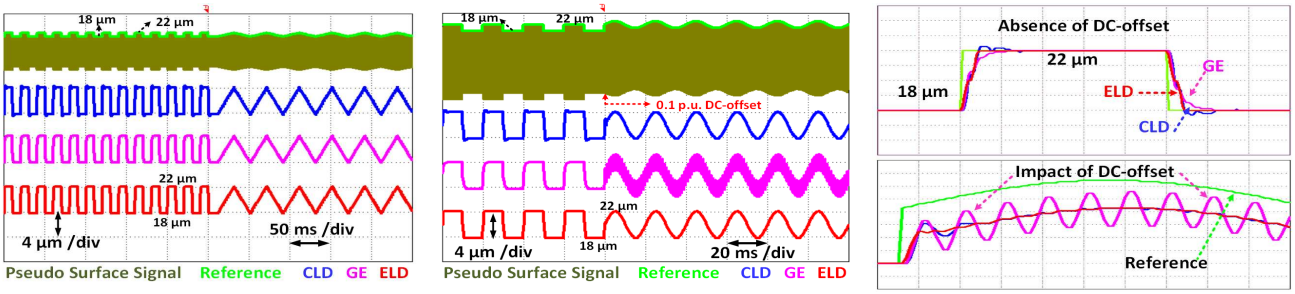
- Amplitude tracking without DC-offset (Fig. 18(a))
- Amplitude tracking with DC-offset (Fig. 18(b))
- Triangular Modulation (Fig. 19(a))
- Sinusoidal Modulation with DC-offset (Fig. 19(b))

The amplitude signal of the pseudo-surface signal is easily detectable by all the estimators in the absence of the DC-offset, as shown in Fig. 18(a). However, the performance of the gradient estimator is severely affected in the presence of DC-offset compared to the proposed ELD and the CLD, as shown in Fig.18(b)-18(c). In addition, the ELD outperforms in terms of settling rapidly to a new-steady state as regards the CLD and the gradient estimator (see Fig. 18(c), magnified view). All the estimators are equally capable of tracking the triangular and/or the sinusoidal amplitude-modulated signals, as shown in Fig. 19(a)-19(b). Note that the proposed ELD ensures faster DC-offset elimination and has a better dynamic response than the CLD and GE, as shown in Fig. 19(c). Hence, it can be inferred that the proposed amplitude estimator has better amplitude tracking capability and a higher degree of DC-offset immunity. It requires the most minor tuning efforts compared to the CLD and GE estimators. The key metrics such as the DC-offset elimination ability, noise rejection ability, steady-state accuracy, applicability, and control complexity of the proposed



(a) Equally spaced pseudo-surface (b) Equally spaced pseudo-surface with DC-offset (c) Case 2: magnified view

Figure 18: Amplitude tracking performance with equally spaced pseudo-surface signal without DC-offset and with DC-offset



(a) Triangular modulation (b) Sinusoidal modulation with DC-offset (c) Case 4: magnified view

Figure 19: Amplitude tracking performance in the presence of a triangular and sinusoidal pseudo-surface amplitude modulation

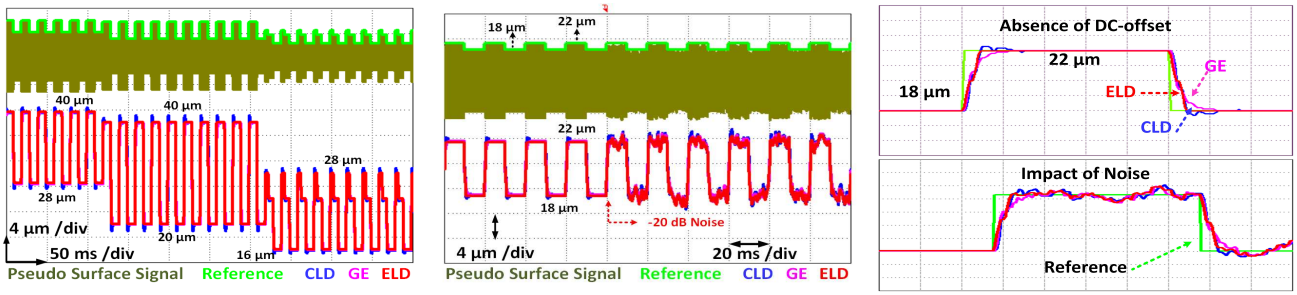
amplitude estimator are compared with the conventional amplitude estimators along with a more recent two-sample based approach (2CS) [15], refer to Table 1. Note that the ELD approach demonstrates better noise suppression ability and steady-state accuracy than the conventional approaches. Compared to the 2CS approach, the amplitude tracking capabilities given low/high-frequency probes AFM application are superior but at the cost of slightly higher control complexity. Furthermore, two additional test cases are reported, which are organized as follows:

- Unequally spaced step variations (Fig. 20(a))
- Equally spaced surface with -20dB noise (Fig. 20(b))

The purpose of these test cases is to present often encountered real-life situations as regards the non-smooth material surfaces [30], as shown in Fig. 20. A test pseudo-surface signal is accordingly generated, demonstrating that the material may have a non-uniform surface and unequal gaps, which might interest structural studies. Therefore, the step decrement in the pseudo-surface signal is considered as shown in Fig. 20(a). It can be observed that all the amplitude estimators can track the step variations in the amplitude signal. Note that the proposed ELD structure and the GE demonstrate higher accuracy in tracing the amplitude information than the CLD structure. Similarly, the measurement accuracy of the AFM instrument may be severely affected by the choice of the working environment. Typically, white Gaussian noise is coupled with the input signal of the measuring device to test the algorithm's performance employed to improve the instrument's performance. In Fig. 20(b), a test pseudo-surface signal is subjected to -20dB of the noise signal, which is later sent to all the amplitude estimators. It can be observed that the impact of noise affects the operation of all the estimators, as shown in Fig. 20(c). However, the noise sensitivity of the CLD estimator is slightly higher than the ELD and GE estimators.

6. Conclusion

This article discusses two samples' potential amplitude tracking abilities based on enhanced Lyapunov's demodulation approach. The modification applied to the conventional



(a) Unequally spaced surface with step variations (b) Equally spaced pseudo-surface with Noise (c) Case 6: magnified view

Figure 20: Amplitude tracking performance in the presence of step variations and noise in the pseudo-surface

Lyapunov approach using delay operators has significantly improved the dynamic response time and addressed the DC-offset issue without any additional feedback loops. Consequently, a faster dynamic response is achieved with ELD and its variants. Also, there is scope to accommodate additional noise-suppressing filters in the ELD structure according to the requirements of the AFM application. It is important to stress that the proposed ELD approach benefits both the low and the high-frequency AFM probes without applying tedious tuning efforts. The experimental results corroborate that the proposed ELD amplitude tracker outperforms the difficulties faced by the CLD and the gradient estimator approach. Hence, the proposed ELD estimator is a suitable choice for AFM application.

Acknowledgement

Dr. Claudio Burgos-Mellado thanks the support of "Agencia Nacional de Investigación y Desarrollo (ANID)" under Grant ANID/ FONDECYT Iniciación/11220989 and Dr. Diego Muñoz-Carpintero thanks the support of "Agencia Nacional de Investigación y Desarrollo (ANID)" under Grant ANID/ FONDECYT Iniciación/11221230.

References

[1] S. K. Das, F. R. Badal, M. A. Rahman, M. A. Islam, S. K. Sarker, N. Paul, Improvement of alternative non-raster scanning methods for high speed atomic force microscopy: A review, IEEE Access 7 (2019) 115603–115624.

[2] Y. S. Hamed, K. M. Albogamy, M. Sayed, A proportional derivative (PD) controller for suppression the vibrations of a contact-mode AFM model, IEEE Access 8 (2020) 214061–214070. doi:10.1109/ACCESS.2020.3038150.

[3] S. Delgado, M. Moreno, L. F. Vázquez, J. Martíngago, C. Briones, Morphology clustering software for AFM images, based on particle isolation and artificial neural networks, IEEE Access 7 (2019) 160304–160323. doi:10.1109/ACCESS.2019.2950984.

[4] D. Y. Abramovitch, S. B. Andersson, L. Y. Pao, G. Schitter, A tutorial on the mechanisms, dynamics, and control of atomic force microscopes, in: 2007 American Control Conference, IEEE, 2007, pp. 3488–3502.

[5] D. Y. Abramovitch, Low latency demodulation for atomic force microscopes, part I efficient real-time integration, in: Proceedings of the 2011 American Control Conference, IEEE, 2011, pp. 2252–2257.

[6] B. Schlecker, A. Nievergelt, M. Ortmanns, G. Fantner, J. Anders, An analog high-speed single-cycle lock-in amplifier for next generation AFM experiments, in: 2018 IEEE Sensors, IEEE, 2018, pp. 1–4.

[7] S. Belikov, J. Alexander, M. Surtchev, S. Magonov, Digital Q-control and automatic probe landing in amplitude modulation phase imaging AFM mode, IFAC-PapersOnLine 50 (1) (2017) 10882–10888.

[8] A. P. Nievergelt, S. H. Andany, J. D. Adams, M. T. Hannebelle, G. E. Fantner, Components for high-speed atomic force microscopy optimized for low phase-lag, in: 2017 IEEE International Conference on Advanced Intelligent Mechatronics (AIM), IEEE, 2017, pp. 731–736.

[9] J. Pérez-Bailón, B. Calvo, N. Medrano, A CMOS low pass filter for SoC lock-in-based measurement devices, Sensors 19 (23) (2019) 5173.

[10] G. Wang, S. Reboul, J.-B. Choquel, E. Fertein, W. Chen, Circular regression in a dual-phase lock-in amplifier for coherent detection of weak signal, Sensors 17 (11) (2017) 2615.

[11] Y. Fang, Y. Zhang, N. Qi, X. Dong, AM-AFM system analysis and output feedback control design with sensor saturation, IEEE Transactions on Nanotechnology 12 (2) (2013) 190–202.

[12] K. Karvinen, S. R. Moheimani, A high-bandwidth amplitude estimation technique for dynamic mode atomic force microscopy, Review of Scientific Instruments 85 (2) (2014) 023707.

[13] V. Kaura, V. Blasko, Operation of a phase locked loop system under distorted utility conditions, IEEE Transactions on Industry Applications 33 (1) (1997) 58–63. doi:10.1109/28.567077.

[14] M. Ayat, M. A. Karami, S. Mirzakuchaki, A. Beheshti-Shirazi, Design of multiple modulated frequency lock-in amplifier for tapping-mode atomic force microscopy systems, IEEE Transactions on Instrumentation and Measurement 65 (10) (2016) 2284–2292.

[15] D. Lagrange, N. Mauran, L. Schwab, B. Legrand, Low latency demodulation for high-frequency atomic force microscopy probes, IEEE Transactions on Control Systems Technology 29 (5) (2021) 2264–2270. doi:10.1109/TCST.2020.3028737.

[16] M. Poik, D. Kohl, M. Mayr, C. Kerschner, G. Schitter, A mechatronic lock-in amplifier: Integrating demodulation in sensor electronics for measuring mechanical oscillations, IEEE Transactions on Instrumentation and Measurement 70 (2021) 1–8. doi:10.1109/TIM.2020.3047208.

[17] M. G. Ruppert, K. S. Karvinen, S. L. Wiggins, S. R. Moheimani, A Kalman filter for amplitude estimation in high-speed dynamic mode atomic force microscopy, IEEE Transactions on Control Systems Technology 24 (1) (2016) 276–284.

[18] M. G. Ruppert, D. M. Harcombe, S. R. Moheimani, High-bandwidth demodulation in mf-afm: A kalman filtering approach, IEEE/ASME Transactions on Mechatronics 21 (6) (2016) 2705–2715.

[19] M. S. Haghighi, M. Sajjadi, H. N. Pishkenari, Model-based topography estimation in trolling mode atomic force microscopy, Applied Mathematical Modelling 77 (2020) 1025–1040.

[20] P. Huang, S. B. Andersson, On detection and estimation in atomic force microscopy at different scan speeds, in: IFAC Symposium on Mechatronics, 2013, pp. 153–160.

[21] M. R. Ragazzon, M. G. Ruppert, D. M. Harcombe, A. J. Fleming, J. T. Gravdahl, Lyapunov estimator for high-speed demodulation in dynamic mode atomic force microscopy, IEEE Transactions on Control Systems Technology 26 (2) (2018) 765–772.

[22] D. M. Harcombe, M. G. Ruppert, M. R. Ragazzon, A. J. Fleming, Lyapunov estimation for high-speed demodulation in multifrequency atomic force microscopy, Beilstein Journal of Nanotechnology 9 (1) (2018) 490–498.

[23] H. Ahmed, M. Benbouzid, Gradient estimator-based amplitude estimation for dynamic mode atomic force microscopy: Small-signal modeling and tuning, Sensors 20 (9) (2020) 2703.

[24] H. Ahmed, Z. Tir, A. K. Verma, S. B. Elghali, M. Benbouzid, Quasi type-1 PLL with tunable phase detector for unbalanced and distorted three-phase grid, IEEE Transactions on Energy Conversion 37 (2) (2022) 1369–1378. doi:10.1109/TEC.2021.3130492.

[25] M. R. P. Ragazzon, S. Messineo, J. T. Gravdahl, D. M. Harcombe, M. G. Ruppert, The generalized lyapunov demodulator: High-bandwidth, low-noise amplitude and phase estimation, IEEE Open Journal of Control Systems 1 (2022) 69–84. doi:10.1109/OJCSYS.2022.3181111.

[26] P. A. Ioannou, J. Sun, Robust adaptive control, Courier Corporation, 2012.

[27] M. L. Pay, H. Ahmed, Modeling and tuning of circular limit cycle oscillator FLL with preloop filter, IEEE Transactions on Industrial Electronics 66 (12) (2019) 9632–9635. doi:10.1109/TIE.2019.2892677.

[28] A. K. Verma, C. Subramanian, R. K. Jarial, P. Roncero-Sánchez, U. M. Rao, A robust lyapunov's demodulator for tracking of single-/three-phase grid voltage variables, IEEE Transactions on Instrumentation and Measurement 70 (2021) 1–11. doi:10.1109/TIM.2020.3043494.

[29] R. G. Lyons, Understanding Digital Signal Processing, Pearson, 2011.

[30] V. Kocur, V. Hegrová, M. Patočka, J. Neuman, A. Herout, Correction of afm data artifacts using a convolutional neural network trained with synthetically generated data, Ultramicroscopy 246 (2023) 113666. doi:10.1016/j.ultramic.2022.113666.